ARTICLE

Check for updates

Subpolar Atlantic Ocean mixed layer heat content variability is increasingly driven by an active ocean

Simon A. Josey [1✉] & Bablu Sinha[1]

Cold conditions in the upper layer of the subpolar North Atlantic Ocean, at a time of pervasive warming elsewhere, have provoked significant debate. Uncertainty arises both from potential causes (surface heat loss and ocean circulation changes) and characteristic timescales (interannual to multidecadal). Resolution of these uncertainties is important as cold conditions have been linked to recent European weather extremes and a decline in the Atlantic overturning circulation. Using observations, supported by high resolution climate model analysis, we show that a surprisingly active ocean regularly generates both cold and warm interannual anomalies in addition to those generated by surface heat exchange. Furthermore, we identify distinct sea surface temperature patterns that characterise whether the ocean or atmosphere has the strongest influence in a particular year. Applying these new insights to observations, we find an increasing role for the ocean in setting North Atlantic mixed layer heat content variability since 1960.

[1] National Oceanography Centre, Southampton SO14 3ZH, UK. ✉email: simon.josey@noc.ac.uk

The surface and upper (0–500 m) layers of the subpolar North Atlantic (SPNA) have exhibited notable spatially coherent temperature anomalies across a broad range of timescales[1–5]. Extreme cold conditions characterised the middle years (2014–2016) of the past decade and have been linked to severe winter surface cooling[2,6–8]. In contrast, SPNA temperatures were particularly warm in the mid-1990s and have been related to changes in both the Atlantic Meridional Overturning Circulation (AMOC)[9,10] and the wind-driven circulation[11–13]. At centennial timescales, the SPNA has experienced reduced warming relative to the rest of the globe, a feature referred to as the 'warming hole'[1]. There is potential for confusion between the cold conditions arising from interannual variability, particularly in 2014–2015, with the signal from the warming hole as they exhibit similar anomalous patterns in sea surface temperature (SST)[7]. More generally the causes of cold and warm SPNA anomalies at interannual timescales are still not well understood and that is the focus of the present study. Our main goal is to understand the extent to which surface heat exchange and ocean heat transport (OHT) are responsible for year-to-year changes in mixed layer heat content and determine whether this balance has changed over the past century.

The balance between variations in ocean heat convergence and heat loss through the air-sea interface lies at the heart of the complex mechanism that determines SST and mixed layer heat content[14–17]. In our analysis, we first consider the sea surface, for which the long-standing Bjerknes conjecture states that atmospheric variability dominates air-sea heat flux and SST changes at interannual timescales, and that the ocean only plays a strong role at longer decadal timescales[18,19]. We test whether the interannual component of the conjecture can still be considered valid by analysing SST variability. Then we shift focus from the sea surface to the mixed layer and explore the relative roles of surface heat exchange and ocean heat convergence in setting its heat content. Variations in the energy made available from the ocean heat content (OHC) reservoir can significantly modify atmospheric dynamics and downstream European weather; including the dominant winter mode of variability[20] and summer heatwaves[2,5,21]. We exploit observations and high-resolution-coupled climate model output to establish the strong role played by OHT variability in setting the mixed layer heat content at interannual timescales. Furthermore, we use a century-long SST based reconstruction to reveal that, over the past 60 years, interannual variability of SPNA mixed layer heat content is increasingly being caused by changes in ocean transport rather than surface heat exchange.

Results

Surface temperature extremes. Ocean surface temperature reaches a minimum in March in the extratropical Northern Hemisphere. Thus, we have computed a measure of interannual variability by taking the difference (ΔSST) of March SST between successive years. Considering the well-observed epoch 1990–2019, the most extreme interannual changes occur from 1995–1996 (warming) and 2013–2014 (cooling). Between March 1995 and March 1996, a major warming event extends across much of the central and eastern SPNA (Fig. 1a). What mechanism drove this interannual change? The Bjerknes conjecture requires it to be due primarily to anomalous air-sea heat transfer. However, the observed 1995–1996 surface net heat flux anomaly is close to zero, $Q'_{n9596} = 3 \pm 2\,\mathrm{W\,m^{-2}}$ (see Fig. 1 caption for full Q'_{n9596} definition). Thus, the event sits outside the Bjerknes paradigm for drivers of interannual variability indicating that variations in OHT must have played a major role in its generation as has been suggested by ocean model analysis[10]. These variations may involve both

horizontal and vertical heat transport, and the vertical heat transports may be related to re-emergence of atmospherically forced anomalies from previous winters. In contrast, the 2013–2014 cooling event (Fig. 1b), occurs during a period of intense heat loss[7], $Q'_{n1314} = -20 \pm 2\,\mathrm{W\,m^{-2}}$. Given the extreme heat loss, this event is potentially consistent with the Bjerknes conjecture. To determine whether the interannual component of the conjecture can still be considered valid we carry out a correlation analysis of ΔSST with Q'_n using the set of March–March events within the period 1990–2019 (see Supplementary Note 1). The analysis shows that the sign of the correlation is positive over the SPNA. However, the ΔSST variance explained by Q'_n typically lies in the range 20–50% that implies that ocean processes (vertical mixing, variations in horizontal heat transport convergence) must also make a significant contribution to the SST variability[19,22]. Thus, the Bjerknes Conjecture does not hold at interannual timescales in the SPNA.

In addition to the 1995–1996 event, the variance results noted above suggest that changes in OHT, rather than surface heat flux, are important for interannual variations in ocean surface temperature on other occasions in the SPNA. For further insights, we extend our analysis by considering the ocean mixed layer heat content. It has been established that heat transport variability can take a leading role in other regions of the global ocean particularly in the Tropics and western boundary current regimes[14,16,23,24]. However, the balance of terms for the mixed layer heat budget in regions of strong water mass transformation like the SPNA[25] remains unclear. In particular, the cause of specific year to year changes in mixed layer heat content, that we consider here, has not yet been established as earlier analyses[14,16] have taken a climatologically fixed depth. These analyses provided valuable advances regarding the causes of variability in the fixed depth upper OHC. However, a mixed layer study needs to take variations in the layer depth from year to year into account and this is a central element of our approach (see Supplementary Note 2 regarding the importance of considering mixed layer depth variability). The SPNA is a region of intense interannual winter heat loss variability[7] and thus one in which the mixed layer heat content may be expected to be largely set by the atmosphere. However, contrary to this expectation, in the next section, we show through analysis of mixed layer heat content variability that surprisingly the OHT plays as strong a role as the surface heat exchange.

Drivers of ocean heat content variability. To examine the role of the ocean further, it is necessary to move beyond SST and consider the heat budget of the mixed layer in the upper ocean which, by definition, has close to the same temperature as the surface[26]. We determine the change (ΔOHC) in March mixed layer OHC between successive years, using a variable mixed layer depth approach, and compare with the integrated net heat flux anomaly ($\int Q'_n$) over the intervening period. The corresponding change (ΔOHT) in the combined lateral and vertical OHT into the mixed layer is then determined by the difference of the two observed quantities (ΔOHT = ΔOHC – $\int Q'_n$, see Methods). This term represents the combined contributions of a range of processes including diffusive mixing, advection and mixed layer depth variations.

This approach is applied separately to two regions covering the NE (55–65 °N, 40–10 °W) and SE (45–55 °N, 40–15 °W) SPNA. These regions were chosen to test whether the subsequent results are sensitive to which of the NE or SE SPNA is considered and allow for possible regional variations in the relative contributions from ΔOHT and $\int Q'_n$ (see Supplementary Note 3). In practice, the results obtained for each region are similar when considering the
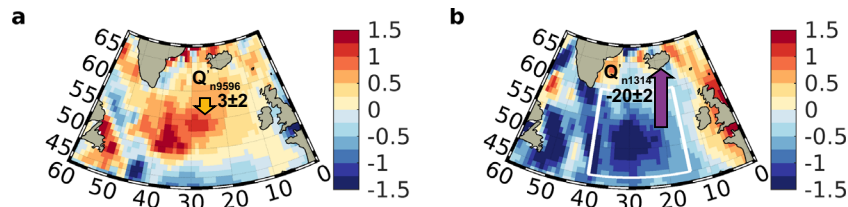
Fig. 1 Interannual North Atlantic surface temperature change. Difference in late winter SST (°C) between successive years **a** March 1996 minus March 1995; **b** March 2014 minus March 2013, source the HadISST[55] dataset. Net heat flux anomalies (Q'_n) are shown by the arrows, positive is ocean heat gain from the atmosphere, negative is heat loss (Wm^{-2}, averaging region 45–60 °N, 40–15 °W, white box, source the NCEP/NCAR[28] atmospheric reanalysis). Q'_{n9596} is the monthly net air-sea heat flux anomaly (relative to 1981–2010) averaged over March 1995 to February 1996; likewise for Q'_{n1314} but for March 2013 to February 2014.

full set of yearly changes although different behaviour can occur in individual years. The UKMO EN4[27] dataset is used to determine ΔOHC and the NCEP/NCAR[28] atmospheric reanalysis for $\int Q'_n$. Consistency with the SST variability is observed, as the strongest warming in the entire 30 year period 1990–2019 occurs between March 1995 and March 1996 in both regions ($\Delta OHC_{NE} = 2.6 \pm 0.1$ ZJ, $\Delta OHC_{SE} = 2.1 \pm 0.1$ ZJ, 1 ZJ $= 10^{21}$ J). Note that here, and subsequently, we use the terms 'warming'/ 'cooling' for brevity to refer to an increase/decrease in OHC, which can be brought about by changes in both temperature and mixed layer volume (see Supplementary Note 4). The 1995–1996 warming cannot be explained by observations of the integrated surface net heat flux ($\int Q'_{nNE} = 0.6 \pm 0.1$ ZJ, $\int Q'_{nSE} = -0.1 \pm 0.1$ ZJ). For both regions, ΔOHC is much larger than $\int Q'_n$. Thus, the 1995–1996 warming must have been driven nearly entirely by increased OHT ($\Delta OHT_{NE} = 2.0 \pm 0.2$ ZJ, $\Delta OHT_{SE} = 2.2 \pm 0.1$ ZJ).

To explore whether the ocean takes an active role in other years, we plot the variation of ΔOHT with $\int Q'_n$ for all individual March–March periods from 1990–2019 (Fig. 2). The March 1995–1996 warming is not the only occasion on which the ocean plays an active role. For the SE SPNA, $|\Delta OHT| > |\int Q'_n|$ in 7 out of 18 years with strong events ($|\Delta OHT|$ or $|\int Q'_n| > 0.5$ ZJ); similar results (8 out of 19 years) are obtained for the NE SPNA. Thus, the active ocean controls near-surface ocean temperature variability in about 40% of the strong events.

These occasions include notable cold (as well as warm) anomalies. In particular, from March 1994–1995, 76% of NE SPNA heat content change is due to the ocean ($\Delta OHC_{NE} = -1.7 \pm 0.1$ ZJ, $\Delta OHT_{NE} = -1.3 \pm 0.2$ ZJ, $\int Q'_{nNE} = -0.4 \pm 0.1$ ZJ). The most extreme case of surface cooling driven change in OHC is March 2013–14 in the SE SPNA which is consistent with the intense heat loss known to have occurred during this winter[7]. When the full set of all year-on-year changes is considered, a more complex picture than the traditional one-way atmosphere-led control emerges. Instead, a two-way balance holds in which the ocean is frequently active in setting its own mixed layer heat content variability rather than passively responding to the atmosphere.

Additional insight into the balance between ocean and atmosphere-led control is provided by analysis of a 100-year climate simulation with the high-resolution HadGEM3.1 model (Fig. 3, see Methods for model details). The increase in resolution of this model compared to earlier models enables significantly better representation of Atlantic OHT and SPNA circulation[29,30]. Here, we find an active role for the ocean in the simulation consistent with the observation-based results discussed above. In particular, for the SE SPNA, $|\Delta OHT| > |\int Q'_n|$ in 43 out of 72 years with strong events ($|\Delta OHT|$ or $|\int Q'_n| > 0.5$ ZJ). Similar results are obtained for the NE SPNA ($|\Delta OHT| > |\int Q'_n|$ in 39 out of 63 strong event years).

Furthermore, the simulation reveals that the degree to which OHC anomalies are set by OHT variability can change
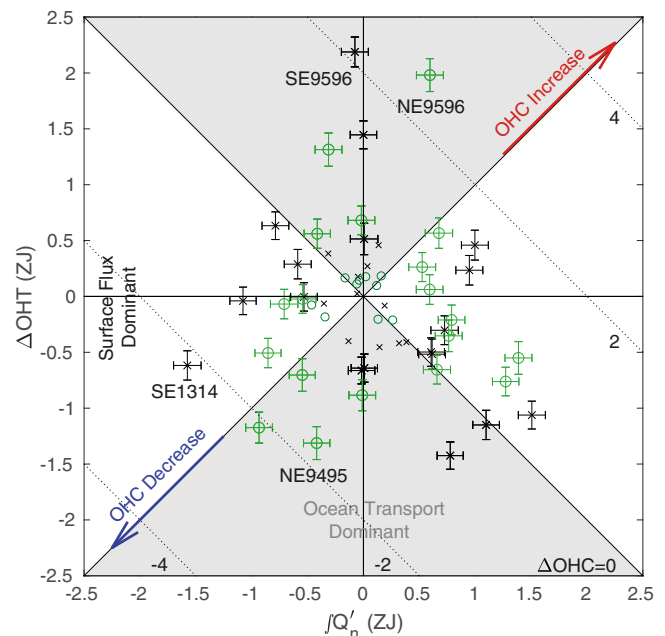

Fig. 2 Ocean transport and surface flux contributions to ocean heat content change. Interannual change in ocean heat transport (ΔOHT) against net heat flux anomaly ($\int Q'_n$) for SE (black crosses) and NE (green circles) SPNA, all years 1991–2019. Labelled lines indicate ocean heat content change ($\Delta OHC = \Delta OHT + \int Q'_n$), units ZJ. Red (blue) arrows show increasing (decreasing) OHC. Shading indicates ocean transport dominance (grey, $|\Delta OHT| > |\int Q'_n|$) and surface flux dominance (white, $|\int Q'_n| > |\Delta OHT|$). One standard deviation error bars included for $|\Delta OHT|$ or $|\int Q'_n| > 0.5$ ZJ. Symbol labels denote specific events, e.g., SE9596 is SE region March 1996 minus March 1995.

substantially between different decades. Specifically, ΔOHT is the lead term in only 2 years for model years (MY) 10–19 but in 7 years for MY 70–79 during which period OHT variability is particularly strong (Fig. 3a). For the century-long span of the run, the level of interannual variability in OHC as measured by the standard deviation of all individual March–March ΔOHC values is $\sigma_{\Delta OHC} = 0.93$ ZJ. However, for a given decade, $\sigma_{\Delta OHC}$ varies from 0.69 to 1.38 ZJ, i.e., the level of interannual variability in OHC can vary by a factor of two depending on the decade under consideration (Fig. 3b).

The variability in model OHC is driven more strongly by changes in OHT ($\sigma_{\Delta OHT} = 0.79$ ZJ) than the surface flux ($\sigma_{\int Q'_n} = 0.58$ ZJ) reflecting the active role of the ocean in the model run. Standard deviations obtained using the same method from the shorter observational record are similar to those found with the model (Fig. 3b, triangles) as is the amplitude of
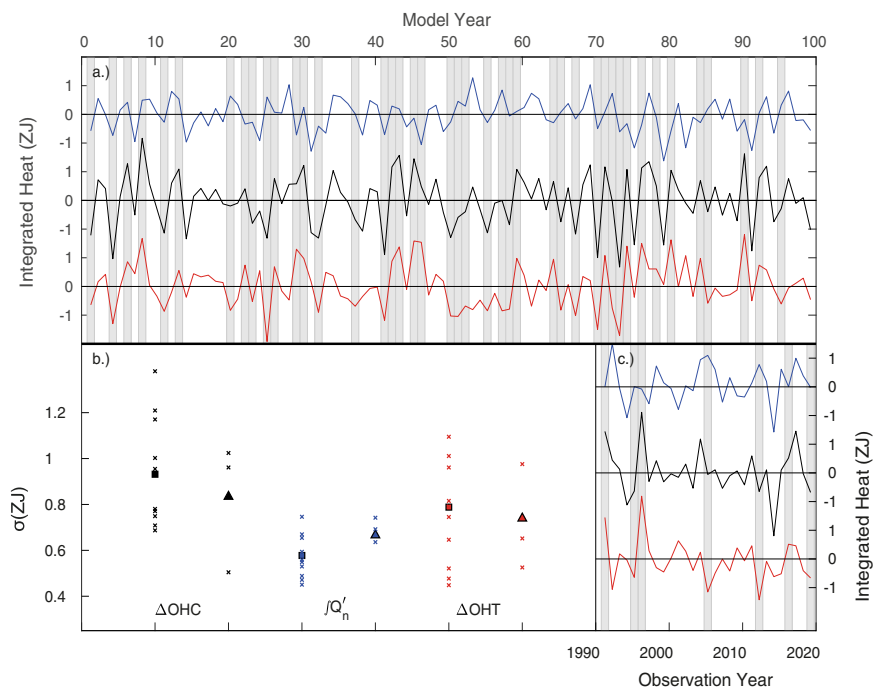
Fig. 3 Time series of modelled and observed ocean heat budget components. a Interannual variation of SE SPNA components from HadGEM3.1 simulation: ΔOHC (black), ΔOHT (red) and $\int Q'_n$ (blue). Grey shading indicates active ocean events ($|\Delta OHT| > |\int Q'_n|$ and $|\Delta OHT| > 0.5$ ZJ). **b** Standard deviation (σ) of all individual March–March ΔOHC, $\int Q'_n$ and ΔOHT values for the full 100-year model simulation (filled squares) and individual decades (crosses). Values determined with the same method from observations for 1990–2019 (filled triangles and crosses). **c** as (**a**) but from observations, note the same approach is used to determine ΔOHT for both the model and observations (see Methods).

variability in the observed time series (Fig. 3c, note any correspondence between the model and observed time series is coincidental as the model is a control run). Thus, both a heat conserving state-of-the-art coupled climate model and observation-based estimates are in agreement regarding drivers of SPNA heat content variability. Each reveals a strong role for the active ocean in regularly driving warm and cold OHC events.

Increasing role for the active ocean. We now explore whether SST responds differently to OHT and surface flux dominant conditions through a composite analysis of observed ΔSST for 1990–2019. The composite method selects on years with $|\int Q'_n| >$ $|\Delta OHT|$ for Fig. 4a (12 data points) and $|\Delta OHT| > |\int Q'_n|$ for Fig. 4b (11 data points). In each case a threshold of 0.5 ZJ has to be exceeded for a given year to be selected (the results are not sensitive to this choice of threshold, see Supplementary Note 5). Both negative and positive events are included but with a scaling factor of -1 applied to the positive events as detailed in the Methodology. The effects of $\int Q'_n$ and ΔOHT dominant conditions on surface ocean temperature can clearly be seen (Fig. 4, note the figure shows the surface temperature change for increased heat loss in Fig. 4a and reduced OHT in Fig. 4b). The composite ΔSST field for the subset of years with $\int Q'_n$ dominant shows a broad region of anomalously cold surface temperature change over much of the basin north of 40 °N consistent with the pattern expected from cold air temperature anomalies associated with north-westerly airflow such as occurred in winter 2013–2014[6]. In contrast, the composite ΔSST field for ΔOHT dominant conditions has a north-south split with cold (warm) ΔSST north (south) of 50 °N. This split is consistent with a reduction in northward heat transport and a consequent deficit (accumulation) of heat at higher (lower) latitudes.

These results provide characteristic SST signatures of strong $\int Q'_n$ and ΔOHT within the modern era. In addition, they potentially enable historical SST data to be used to reconstruct the contributions of OHT and surface heat flux to interannual mixed layer heat content variability over the past 150 years. Such an approach is of particular value as SST observations are available back to 1870 via HadISST but reliable Q_n and OHT observations are not.

To carry out the reconstruction, the contrasting ΔSST patterns have been used to define index values, I_{Qn} and I_{OHT}, for $\int Q'_n$ and ΔOHT dominant conditions. I_{Qn} is the regional mean of ΔSST for the box spanning the cold eastern SPNA pattern in Fig. 4a normalised by its standard deviation for 1870–2019. I_{OHT} is the corresponding north-south difference of normalised ΔSST for two smaller boxes centred on the poles of the ΔSST pattern associated with ΔOHT dominance (Fig. 4b). Time series of I_{Qn} and I_{OHT} show strong interannual variability with some indication that the amplitude of the ΔOHT contribution increases and that of the $\int Q'_n$ contribution decreases in the second half of the record (Fig. 4c). We have quantified this using the mean magnitude of the 10 most extreme values for I_{Qn} and I_{OHT} before and after 1960. In each case, the difference in values between the two periods exceeds the error: I_{Qn} (pre-1960) = 2.19 ± 0.15, I_{Qn} (post-1960) = 1.65 ± 0.10; I_{OHT} (pre-1960) = 1.77 ± 0.14, I_{OHT} (post-1960) = 2.12 ± 0.16.

To explore this further, we determine moving means of the absolute index values and these reveal notable variability in the relative strength of I_{Qn} and I_{OHT} (Fig. 4d). From 1870 to about 1960, they tend to be similar in magnitude and strongly correlated ($r = 0.72$, significant at 95% level). However, after 1960 they become decorrelated ($r = -0.15$, not significant) and there are several periods, highlighted in grey, during which I_{OHT} is noticeably larger than I_{Qn}. In these periods, the active ocean
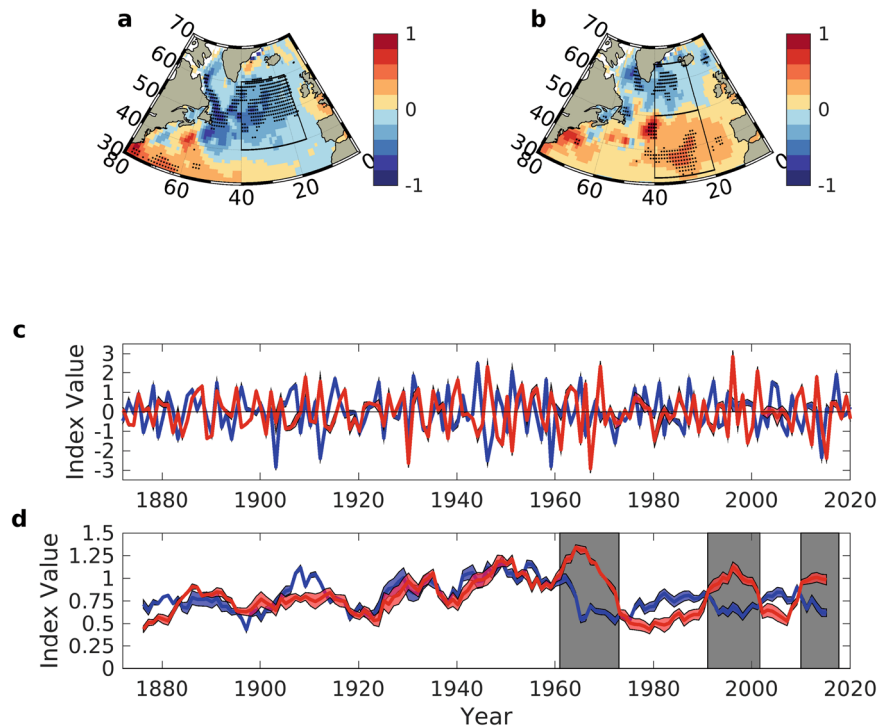
Fig. 4 Observed ΔSST composite maps and pattern time series. Composite mean of ΔSST for **a** $\int Q'_n$ dominant conditions, increased surface heat loss; **b** ΔOHT dominant conditions, reduced ocean heat transport. Stippling indicates 95% significance level. Boxes in **a**, **b** show the index regions for I_{Qn} (40–60 °N, 40–15 °W) and I_{OHT} (50–65 °N, 40–20 °W and 32–50 °N, 40–20 °W). **c** Time series of I_{OHT} (red) and I_{Qn} (blue). **d** Time series of 11-point centred moving average values for $|I_{OHT}|$ (red) and $|I_{Qn}|$ (blue). Grey shading indicates prolonged periods of ΔOHT dominance. Blue and red shadings about solid lines in **c**, **d** indicate uncertainty due to the choice of boxes used to form the different indices (see Methods).

plays the primary role in setting interannual variability of the SPNA mixed layer heat content and the net heat flux contribution is reduced. Thus, the contribution of OHT variability relative to surface heat exchange has become more dominant in the past 60 years. Why is this the case? One possibility is that weakening of the AMOC[31,32] has led to increased instability of the ocean circulation and the amount of heat it transports polewards. In this scenario, rather than staying predominantly in a relatively fixed strong state, the ocean has recently varied more frequently between strong and slightly weaker states at interannual time-scales enabling greater ocean activity in setting SPNA OHC. We stress that this is a possible explanation and that it is important to remember that the change in contribution from the ocean may also include other processes, e.g., vertical mixing. Thus, it is not possible at this point to conclusively associate the change over the past 60 years with a weakening AMOC. In addition, a reduction in the overall severity of cold air outbreaks[33] may have weakened the net heat loss in such events, thus making the mixed layer heat content less sensitive to the surface heat flux. Further research is needed to test these hypotheses, potentially using coupled model ensemble analysis.

Conclusions

Through a combined analysis of SPNA observations and a high-resolution climate model simulation, we have revealed an active role for ocean transports in generating both warm and cold interannual anomalies in mixed layer heat content. Our findings firmly establish that the ocean is frequently active in setting its own mixed layer heat content variability rather than passively responding to the atmosphere. The focus of this study has primarily been interannual variability but our results are also relevant to the ongoing debate about the role of the ocean at interdecadal timescales[19,34–39]. We have found evidence for

variability in the extent of interannual ocean activity from decade to decade. This has the potential to confound attempts to identify robust decadal modes of variability and needs to be considered in such studies. Furthermore, from a reconstruction using SST observations since 1870, we infer that the level of ocean activity relative to surface heat flux has increased markedly over the past 60 years. This points to a possible role for a weakening AMOC (through increased instability of the ocean circulation and the amount of heat it transports polewards) that merits further investigation, particularly as a recent multi-proxy reconstruction indicates a rapid AMOC decline from about 1960[31].

Our results open the door to a clearer understanding of the impacts of variability in the North Atlantic ocean circulation on the coupled ocean-atmosphere system including European weather. Ocean surface and upper layer temperature anomalies have been shown to influence both winter cold events[40–42] and summer heatwaves[2,5] over Europe in model analyses. By integrating our new insights into such studies, it will be possible to examine whether an increasingly active ocean is now playing a greater role in determining European weather events by exerting a tighter control over the mixed layer heat content reservoir available to the atmosphere.

Methods

Heat transport calculation. For a given region, specifically the NE and SE boxes in our study, the change in the amount of heat transported laterally and vertically by the ocean (ΔOHT) into the mixed layer is given by the residual:

$$\Delta\text{OHT} = \iiint \rho c_p (T_{M2} - T_{M1}) dxdydz - \iiint Q'_n \, dxdydt \qquad (1)$$

with ρ, the density of seawater (taken to be 1025 kg m⁻³), c_p, the specific heat capacity of seawater (3850 J kg⁻¹ °C⁻¹), T_{M2}, T_{M1}, the potential temperature in March of year 2 and year 1, respectively, Q'_n the net surface heat flux anomaly integrated over the intervening time period. The first term on the right hand side is

integrated over the mixed layer depth H(x,y,t) where H is defined to be the first depth layer at which the potential temperature is more than 0.5 °C lower than the surface temperature. We stress that, unlike many previous studies, H is calculated for each individual month rather than following a climatological monthly definition and thus takes interannual variability into account.

The approach detailed above is taken for both the observation and model ΔOHT calculations. For the observations, the Q'_n integral, second term, is calculated by summing values of the monthly net air-sea heat flux anomaly, relative to the 1981–2010 seasonal cycle, from March of year 1 to February of year 2 inclusive. For the model, the Q'_n integral is calculated in the same way relative to a seasonal cycle determined from years 31–60 of the 100-year run. Note, earlier studies have considered the combined effects of the net heat flux and wind-driven Ekman transport in a single term[16,23]. However, we treat the net heat flux in isolation and the Ekman contribution is implicitly included within the ΔOHT term. We have explored whether the observed ΔOHT variations can be related to the local wind stress by calculating the convergence of the observed Ekman volume transport into both the SE and NE boxes and correlating with the ΔOHT values for each box from 1991–2019. For the NE box, there is a weak positive correlation ($r = 0.37$, significant at 95%), while the SE box value is close to zero ($r = -0.14$, insignificant at 95%). Although weak these results suggest a possible regional variation with the Ekman contribution becoming important towards the NE of the SPNA. We plan to explore this in subsequent research targeted at the relationship between the wind-driven transport, the air-sea heat flux and ΔOHT.

Definition of ΔOHT or $\int Q'_n$ dominance. In our analysis, we define whether a given year is ΔOHT dominant according to the requirement that $|\Delta OHT| > |\int Q'_n|$. We have also investigated whether using a more stringent requirement that one term needs to be substantially larger than the other impacts our key conclusion that ocean transports are dominant for nearly a half of the cases considered. Specifically, if we require that ΔOHT is larger in magnitude than $\int Q'_n$ by 0.5 ZJ as the condition for dominance then we find that 6 out of 11 years have ΔOHT dominant for the SE region (5 out of 11 for NE). This compares with 7 out of 18 years for the SE region (8 out of 19 for NE) with the simple inequality approach used previously. Thus, including the requirement that one term needs to be substantially larger than the other slightly increases the proportion of ocean transport dominant events such that ΔOHT is dominant for half of the cases considered.

Climate model specification. The 100-year climate simulation has been produced using the HadGEM3-GC3.1 model (Met Office Hadley Centre Global Coupled model General Circulation 3.1) which has an ocean resolution of 1/12° and an N512 (approximately 25 km) atmosphere[43]. HadGEM3-GC3.1 incorporates the GA/GL7.1 global atmosphere–land configuration that uses a regular latitude–longitude grid and has 85 levels extending to 85 km[44]. The global ocean component is GO6[45], which uses the Nucleus for European Modelling of the Ocean model at vn3.6, having a tripolar grid, with 75 ocean levels (and top level thickness of 1 m). The sea ice model configuration is GSI8.1[46], which uses the CICE5.1 model. The model is initialised using a combination of atmospheric reanalysis and ocean/ice output from a lower resolution model simulation consistent with the CMIP6 HighResMIP protocol[47]. Full details of the model configuration and spin up are provided by[48]. By using a coupled model we avoid having to prescribe the surface heat exchange that is necessary in forced ocean models; such models have shown discrepancies in their representation of the eastern SPNA heat budget[49].

Error estimation and composites. Error estimates for ΔOHC have been obtained following the Monte Carlo methodology. For each month, the OHC relative to the 1981–2010 mean is calculated using the EN4 temperature and temperature uncertainty fields. This process is repeated 1000 times with randomly sampled uncertainty values and used to derive the ΔOHC error estimates. The $\int Q'_n$ error estimates are determined using the same 1000 repeat Monte Carlo approach with monthly random errors specified for each of the four component heat flux fields that sum to form the net heat flux. These are the latent (specified error 30 Wm^{-2}), sensible (20 Wm^{-2}), longwave (15 Wm^{-2}) and shortwave (20 Wm^{-2}) fluxes. The error values in brackets are conservative one standard deviation estimates based on evaluations of NCEP/NCAR and other reanalyses using surface flux buoy observations[50,51]. The sensible and latent heat flux errors are potentially strongly interdependent as they are driven by errors in the wind speed and near-surface temperature and humidity gradients; to allow for this possibility the sensible heat flux error is taken to be 2/3 of the latent heat flux error on each repeat. The uncertainties in ΔOHC and $\int Q'_n$ are summed in quadrature to form the error on ΔOHT. All error estimates are specified at the one standard deviation level. Note, as a further consistency check, the surface flux dependent results reported in the paper have been re-determined using an alternative reanalysis, ERA5[52]. Similar results are obtained with either reanalysis. For example, for March 1995 to February 1996 the box integrated net heat flux values with the two datasets both show net warming in the NE box: $\int Q'_n = 0.58$ (0.59) ZJ for ERA5 (NCEP) and both are close to zero in the SE box: $\int Q'_n = 0.11$ (−0.08) ZJ for ERA5 (NCEP).

The ΔSST pattern in Fig. 4a represents surface heat flux dominance over OHT and increased surface heat loss conditions. It shows the composite mean of years with $|\int Q'_n| > |\Delta OHT|$ and $|\int Q'_n| > 0.5$ ZJ (12 members within period 1991–2019). Both negative ($\int Q'_n < -0.5$ ZJ and $\int Q'_n < \Delta OHT$) and positive ($\int Q'_n > 0.5$ ZJ and $\int Q'_n > \Delta OHT$) events are used to form the composite in order to increase the sample size. To prevent cancellation of the ΔSST patterns associated with negative and positive events (which are similar but of opposite sign) a scaling factor of −1 is applied to the patterns from the positive events. The ΔSST pattern in Fig. 4b represents OHT dominance over surface flux and reduced heat transport conditions. It shows the composite mean for years with $|\Delta OHT| > |\int Q'_n|$ and $|\Delta OHT| > 0.5$ ZJ (11 members). As above, both negative ($\Delta OHT < -0.5$ ZJ and $\Delta OHT < \int Q'_n$) and positive ($\Delta OHT > 0.5$ ZJ and $\Delta OHT > \int Q'_n$) events are selected, and ΔSST for those members with $\Delta OHT > 0.5$ ZJ is scaled by a factor −1 for sign consistency with reduced heat transport. Confidence limits for stippling of the composite fields have been determined using the Normal-Z statistic[53]. Values for $\int Q'_n$ and ΔOHT used to select the years that form the composites are calculated for the eastern SPNA (45–65 °N, 40–15 °W). The effective sampling size for testing of correlation significance has been determined according to[54].

Note the boxes used to determine I_{OHT} and I_{Qn} in Fig. 4 are process-based (i.e., specified according to the pattern resulting from OHT or surface heat dominance) and were defined after the analysis used to produce Fig. 4a, b patterns. They are different to the NE and SE boxes used for Fig. 2 that are regional sub-divisions chosen for a sensitivity analysis. We have explored also whether the I_{OHT} and I_{Qn} time series shown in Fig. 4c, d are sensitive to the box definitions employed and find this is not the case. For this sensitivity analysis, each of the box boundaries is varied by 1° steps within a 10° range and the time series are recalculated in each case. The standard deviation of the resulting ensemble of time series is determined and shown by shading about the original results (solid lines) in Fig. 4c, d. It can be seen from the figure that the uncertainty due to possible alternative box definitions is small and our main result that there is a change in the relative behaviour of the time series after 1960 is robust to the choice of boxes used to define the I_{OHT} and I_{Qn} indices.

References

1. Chemke, R., Zanna, L. & Polvani, L. M. Identifying a human signal in the North Atlantic warming hole. *Nat. Commun.* **11**, 1540 (2020).
2. Duchez, A. et al. North Atlantic Ocean drivers of the 2015 European heat wave. *Env. Res. Lett.* **11**, 074004 (2016).
3. de Jong, M. F. & de Steur, L. Strong winter cooling over the Irminger Sea in winter 2014–2015, exceptional deep convection, and the emergence of anomalously low SST. *Geophys. Res. Lett.* **43**, 7106 (2016).
4. Piron, A., Caniaux, G., Mercier, H. & Thierry, V. Gyre-scale deep convection in the subpolar North Atlantic Ocean during winter 2014–2015. *Geophys. Res. Lett.* **44**, 1439 (2017).
5. Mecking, J. V., Drijfhout, S. S., Hirschi, J. J.-M. & Blaker, A. T. Ocean and atmosphere influence on the 2015 European heatwave. *Env. Res. Lett.* **14**, 114035 (2019).
6. Grist, J. P. et al. Extreme air-sea interaction over the North Atlantic subpolar gyre during the winter of 2013-14 and its sub-surface legacy. *Climate Dynamics* **46**, 4027 (2016).
7. Josey, S. A. et al. The recent Atlantic cold anomaly: causes, consequences, and related phenomena. *Ann. Rev. Mar. Sci.* **10**, 475–501 (2018).
8. Dacre, H. F., Josey, S. A. & Grant, A. L. M. Extratropical cyclone induced sea surface temperature anomalies in the 2013/14 winter. *Weather and Climate Dynamics* **1**, 27–44 (2020).

9. Jackson, L. C., Peterson, K. A., Roberts, C. D. & Wood, R. A. Recent slowing of Atlantic overturning circulation as a recovery from earlier strengthening. *Nat. Geosci.* **9**, 518 (2016).

10. Robson, J., Lohmann, K., Palmer, M., Smith, D. & Sutton, R. Causes of the rapid warming of the North Atlantic Ocean in the mid 1990s. *J. Clim.* **25**, 4116 (2012).

11. Bersch, M. North Atlantic Oscillation–induced changes of the upper layer circulation in the northern North Atlantic Ocean. *J. Geophys. Res.* **107**, 3156 (2002).

12. Häkkinen, S. & Rhines, P. B. Decline of subpolar North Atlantic circulation during the 1990s. *Science* **304**, 555–559 (2004).

13. Piecuch, C. G., Ponte, R. M., Little, C. M., Buckley, M. W. & Fukumori, I. Mechanisms underlying recent decadal changes in subpolar North Atlantic Ocean heat content. *J. Geophys. Res. Oceans* **122**, 7181–7197 (2017).

14. Roberts, C. D. et al. Surface flux and ocean heat transport convergence contributions to seasonal and interannual variations of ocean heat content. *J. Geophys. Res. Oceans* **122**, 726 (2017).

15. Moat, B. I. et al. New insights into decadal North Atlantic sea surface temperature and ocean heat content variability from a high-resolution coupled climate model. *J. Clim.* **32**, 6137 (2019).

16. Buckley, M. W., Ponte, R. M., Forget, G. & Heimbach, P. Low-frequency SST and upper-ocean heat content variability in the north Atlantic. *J. Clim.* **27**, 4996 (2014).

17. Small, R. J., Bryan, F. O., Bishop, S. P., Larson, S. & Tomas, R. A. What drives upper-ocean temperature variability in coupled climate models and observations? *J. Clim.* **33**, 577 (2020).

18. Bjerknes, J. Atlantic air-sea interaction. *Adv. Geophys.* **10**, 1 (1964).

19. Gulev, S. K., Latif, M., Keenlyside, N., Park, W. & Koltermann, K. P. North Atlantic Ocean control on surface heat flux on multidecadal timescales. *Nature* **499**, 464 (2013).

20. Grist, J. P. et al. Re-emergence of North Atlantic subsurface ocean temperature anomalies in a seasonal forecast system. *Clim. Dyn.* **52**, 334 (2019).

21. Ossó, A., Sutton, R., Shaffrey, L. & Dong, B. Development, amplification, and decay of Atlantic/European summer weather patterns linked to spring North Atlantic sea surface temperatures. *J. Clim.* **33**, 5939 (2020).

22. O' Reilly, C. H. & Zanna, L. The signature of oceanic processes in decadal extratropical SST anomalies. *Geophys. Res. Lett.* **45**, 7719 (2018).

23. Buckley, M. W., Ponte, R. M., Forget, G. & Heimbach, P. Determining the origins of advective heat transport convergence variability in the north Atlantic. *J. Clim.* **28**, 3943 (2015).

24. Buckley, M. W. & Marshall, J. Observations, inferences, mechanisms of Atlantic Meridional Overturning Circulation variability: a review. *Rev. Geophys.* **54**, https://doi.org/10.1002/2015RG000493 (2016).

25. Petit, T., Lozier, M. S., Josey, S. A. & Cunningham, S. A. Atlantic deep water formation occurs primarily in the Iceland basin and irminger sea by local buoyancy forcing. *Geophys. Res. Lett.* **47**, e2020GL091028 (2020).

26. de Boyer Montégut, C., Madec, G., Fischer, A. S., Lazar, A. & Iudicone, D. Mixed layer depth over the global ocean: an examination of profile data and a profile-based climatology. *J. Geophys. Res.* **109**, C12003 (2004).

27. Good, S. A., Martin, M. J. & Rayner, N. A. EN4: quality controlled ocean temperature and salinity profiles and monthly objective analyses with uncertainty estimates. *J. Geophys. Res.* **118**, C6704 (2013).

28. Kistler, R. et al. The NCEP–NCAR 50-year reanalysis: monthly means CD-ROM and documentation. *Bull. Amer. Met. Soc.* **82**, 247 (2001).

29. Roberts, M. J. et al. Impact of ocean resolution on coupled air-sea fluxes and large-scale climate. *Geophys. Res. Lett.* **43**, 10430 (2016).

30. Hirschi, J. J.-M. et al. The Atlantic Meridional Overturning Circulation in high resolution models. *J. Geophys. Res.* **125**, e2019JC015522 (2020).

31. Caesar, L., McCarthy, G. D., Thornalley, D. J. R., Cahill, N. & Rahmstorf, S. Current Atlantic Meridional Overturning Circulation weakest in last millennium. *Nat. Geosci.* **14**, 118 (2021).

32. Rahmstorf, S. et al. Exceptional twentieth-century slowdown in Atlantic Ocean overturning circulation. *Nat. Clim. Change* **5**, 475 (2015).

33. Smith, E. T. & Sheridan, S. C. Where do cold air outbreaks occur, and how have they changed over time? *Geophys. Res. Lett.* **47**, e2020GL086983 (2020).

34. Robson, J., Polo, I., Hodson, D. L. R., Stevens, D. P. & Shaffrey, L. C. Decadal prediction of the North Atlantic subpolar gyre in the HiGEM high-resolution climate model. *Clim. Dyn.* **50**, 921 (2018).

35. Cane, M. A., Clement, A. C., Murphy, L. N. & Bellomo, K. Low-pass filtering, heat flux, and Atlantic multidecadal variability. *J. Clim.* **30**, 7529 (2017).

36. Arthun, M., Wills, R. C. J., Johnson, H. L., Chafik, L. & Langehaug, H. R. Mechanisms of decadal North Atlantic climate variability and implications for the recent cold anomaly. *J. Clim.* **34**, https://doi.org/10.1175/JCLI-D-20-0464.1 (2021).

37. Bryden, H. L. et al. Reduction in ocean heat transport at 26N since 2008 cools the eastern subpolar gyre of the North Atlantic Ocean. *J. Clim.* **33**, 1677 (2020).

38. Desbruyères, D., Chafik, L. & Maze, G. A shift in the ocean circulation has warmed the subpolar North Atlantic Ocean since 2016. *Commun. Earth Environ.* **2**, 48 (2021).

39. Mann, M. E., Steinman, B. A., Brouillette, D. J. & Miller, S. K. Multidecadal climate oscillations during the past millennium driven by volcanic forcing. *Science* **371**, 1014 (2021).

40. Buchan, J., Blaker, A. T., Hirschi, J. J.-M. & Sinha, B. North Atlantic SST anomalies and the cold North European weather events of winter 2009/10 and December 2010. *Mon. Wea. Rev.* **142**, 922 (2014).

41. Maidens, A. et al. The influence of surface forcings on the prediction of the North Atlantic Oscillation regime of winter 2010-2011. *Mon. Wea. Rev.* **141**, 3801 (2013).

42. Miller, D. E. & Wang, Z. Skillful seasonal prediction of Eurasian winter blocking and extreme temperature frequency. *Geophys. Res. Lett.* **46**, 11530 (2019).

43. Williams, K. D. et al. The Met Office Global Coupled model 3.0 and 3.1 (GC3.0 and GC3.1) configurations. *J. Adv. Model. Earth Syst.* **10**, 357 (2017).

44. Walters, D. et al. The Met Office Unified Model Global Atmosphere 7.0/7.1 and JULES Global Land 7.0 configurations. *Geosci. Model Dev.* **12**, 1909 (2019).

45. Storkey, D. et al. UK Global Ocean GO6 and GO7: a traceable hierarchy of model resolutions. *Geosci. Model Dev.* **11**, 3187 (2018).

46. Ridley, J. et al. The sea ice model component of HadGEM3-GC3.1. *Geosci. Model Dev.* **11**, 713 (2018).

47. Haarsma, R. J. et al. High Resolution Model Intercomparison Project (HighResMIP v1.0) for CMIP6. *Geosci. Model Dev.* **9**, 4185 (2016).

48. Roberts, M. J. et al. Description of the resolution hierarchy of the global coupled HadGEM3-GC3.1 model as used in CMIP6 HighResMIP experiments. *Geosci. Model Dev.* **12**, 4999 (2019).

49. Foukal, N. P. & Lozier, M. S. Examining the origins of ocean heat content variability in the eastern North Atlantic subpolar gyre. *Geophys. Res. Lett.* **45**, 11275 (2018).

50. Bentamy, A. et al. Towards improved estimation of turbulent heat flux over the global oceans. *Remote Sens. Environ.* **201**, 196 (2017).

51. Josey, S. A. A comparison of ECMWF, NCEP/NCAR and SOC surface heat fluxes with moored buoy measurements in the subduction region of the North-East Atlantic. *J. Clim.* **14**, 1780 (2001).

52. Hersbach, H. et al. The ERA5 global reanalysis. *Q. J. Roy. Met. Soc.* **146**, 1999 (2020).

53. Harrison, D. E. & Larkin, N. K. The COADS sea level pressure signal: a near global El Nino composite and time series view, 1946-1993. *J. Clim* **9**, 3025 (1996).

54. Ciasto, L. M. & Thompson, D. W. J. Observations of large-scale ocean–atmosphere interaction in the Southern Hemisphere. *J. Clim.* **21**, 1244–1259 (2008).

55. Rayner, N. A. et al. Global analyses of sea surface temperature, sea ice, and night marine air temperature since the late nineteenth century. *J. Geophys. Res.* **108**, D4407 (2003).

Acknowledgements

Author contributions

S.A.J. conceived the study, carried out the analysis and wrote the manuscript. B.S. undertook the model diagnostic calculations, discussed and interpreted the results and provided input to the manuscript.

Competing interests

The authors declare no competing interests.

Additional information